Master's Thesis

Near-Field Measurement System for 5G Advanced Antenna System at mm-Wavelength

By

Bofei Wang

Department of Electrical and Information Technology
Faculty of Engineering, LTH, Lund University
SE-221 00 Lund, Sweden

Abstract

An antenna is one of the most fundamental elements of wireless communication systems. The radiation behavior of antennas is characterized with the aid of the far-field radiation pattern. In this thesis, a near-field antenna measurement system is designed to predict the far-field pattern of antenna operational frequency 28 GHz and 39 GHz. The near-field measurement system operates by measuring magnitude and phase of the tangential electric field components radiated by antenna under test over a surface in an anechoic chamber and then mathematically transforming using the MATLAB tool into the far-field radiation pattern.

The WR28 standard gain horn antenna is used as an antenna under test and WR28 rectangular waveguide as a probe. The planar scanning geometric was implemented by designing a scanner of length 165 mm x 175 mm and near-field data are measured at specific points based on the sampling values using a Vector Network Analyzer (VNA) in an anechoic chamber. The near-field to far-field transformation is implemented using the Plane Wave Spectrum (PWS) method by Fourier transforms in MATLAB. The measurements were performed for different separation distances between the antennas, sampling value, and reasonably accurate results are observed.

Acknowledgments

I would like to express my sincere gratitude towards Mats Gustafsson and Martin Torleif for their expertise and guidance for the thesis project.

I would also like to thank Muhammad Waqas Ahmad Khan and David Lundberg for giving me the opportunity to conduct this thesis at Ericsson and for taking a keen interest in guiding all along with the thesis.

I would also like to express immense gratitude towards my family and friends for their continuous support during the master's program.

Finally I would thanks my project's partner and friend Srinivas Dhoola for the contributions and nice work during the thesis project.

Bofei Wang

Table Contents

List of Figures

List of Tables

Acronyms

NR	New Radio
AAS	Advanced Antenna System
MIMO	Multiple Input Multiple Output
IC	Integrated Circuit
OTA	Over the Air
3GPP	3rd Generation Partnership Project
PEC	Perfect Electric Conductor
PMC	Perfect Magnetic Conductor
CATR	Compact Antenna Test Ranges
AUT	Antenna Under Test
NFTFF	Near-Field to Far-Field
FFT	Fast Fourier Transform
OERWG	Open-Ended Rectangular Waveguide
NF	Near-Field
FF	Far-Field
PWM	Pulse Width Modulation
IDE	Integrated Development Environment
VNA	Vector Network Analyzer
GPIB	General Purpose Interface Bus
USB-HS	Universal Serial Bus-High Speed

1

Introduction

An antenna radiation field pattern can be obtained from near-field or far-field ranges [1]. For lower frequency antennas and simple pattern cut measurements, the far-field ranges are a better choice. The near-field ranges are more suitable for higher frequency antennas, full pattern and polarization measurements. Depending on the cost, complexity, and dimension of the antenna the measurement type is chosen. This chapter provides a brief overview of the project.

1.1 Background

The mobile communication industry has risen tremendously over the previous decade, and it is expected to grow with more devices being connected every day, according to Ericsson's statistics and forecast[2], 1.0billion devices with cellular at end of 2018 and there will be 4.1 billion cellular IoT connected devices in 2024. In the upcoming 5G New Radio (NR), to achieve a higher data rate and capacity, Active Antenna System (AAS) [3] system technology is used. AAS is a multiantenna feature that includes beamforming, Multiple Input Multiple Output (MIMO) and enhances network performances significantly in both uplink and downlink. Beamforming is the ability to direct narrow beams (by adjusting the phase and amplitude of a signal applied to each antenna) toward a specific direction, means the antenna has good directivity so that it can improve the spectral efficiency also the signal to noise ratio. MIMO technology is used to increase throughput by using the same time and frequency resources while transmitting multiple data streams. Since mm-wave has

higher propagation loss, multiple AAS systems are used in overall 5G systems for good coverage and to compensate for the loss.

In AAS, an antenna array, radio chains and parts of the baseband, all tightly integrated with a high level of integration and may not be able to physically expose a cable connector or probe points to the test equipment. Thus, putting the need of Over the Air (OTA) testing [4]. The performance of the antenna array itself and the connection between the antenna array and the Radio Frequency (RF) transceivers are critical, the performance evaluation of AAS needs to have antenna array included, which needs the OTA test methodologies [5]. OTA measurements are the standardized methods to evaluate radio performance in wireless systems. These measurements are typically performed in either the near-field or the far-field regions of the testing antenna [4].

The 3GPP [6] has approved the following test methods to date: direct far-field, indirect far-field or Compact Antenna Test Ranges (CATR) and near-field to far-field transform (or near-field). Depending on the device architecture, antenna size and configuration the test methods are chosen. Because of space and cost demand, the direct far-field method isn't viable. The CATR and the near-field test methods are being actively testing to enable and support all the measurement needs at a reasonable cost and space.

1.2 Aim

The goal of this master thesis is to design a near-field antenna measurement system to determine the far-field radiation pattern of Ericsson's 5G NR system. The system should operate at frequency 28 GHz or 39 GHz and be able to measure the radiation pattern E-plane and H-plane of the antenna.

The scope of the thesis work can be divided into three major milestones. Firstly, selection of techniques suitable for 5G NR. Secondly, the study, selection of components to build the system. Thirdly, building the chamber and testing the methods for basic horn antenna for accuracy of the system in Ericsson AB, Lund.

1.3 Limitations

Compact Antenna Test Ranges (CATR) is work focused on a specific antenna system of 5G NR developed by Ericsson. The near-field system is designed for Ericsson's 5G NR, but owing to time limitations, the system is tested for a horn antenna. The results will be published in two different forms:

- The complete version presented only to Ericsson.
- A basic edited version opens and available to everyone.

1.4 Challenge

After research to build this system may face a lot of challenges. Those challenges will be the success key to our project. If we managed these challenges well the project will be easier.

- Choosing a suitable probe to measure. Need to balance the performance and budgets and get a suitable probe.
- Build a mechanics system controlled by Arduino. Few experiences on this, would take more time.
- Positioning. Because we are measuring mm-wave antenna, some small positioning error will lead a big measurement difference.
- Small Anechoic Chamber. Should determine the dimension of measurement area and build a proper chamber.
- Near Field to Far Field transformation. This requires a lot of mathematics knowledge to understand and implement.
- Accuracy. A lot of issues will influence the results' accuracy. Like positioning we mentioned before, also environment radiation, devices' accuracy and so on.

1.5 Outline

The next chapters of this report are structured as follows. In chapter 2, an overview of fundamental concepts for the project. Chapter 3 shows the design and implementation of the hardware and software of the system. Chapter 4 presents the simulations and results of the model. In the final chapter, conclusions of the designed system and suggestions for future work is prefer.

2

Theoretical Background

The antenna is a means for radiating or receiving electromagnetic waves and is an important element for a wireless communication system [7]. Antennas transmit and receive the signal in the same radiation pattern due to their reciprocity property. The signal will radiate from the antenna, depending on the frequency, phase, and amplitude of the signal and the antenna features. In this chapter, an overview of various characteristics of antenna essential for the thesis is described.

2.1 Field regions

The antenna radiated electromagnetic field distribution changes gradually with the distance and are categorized into three regions [7]: reactive near-field, radiating near-field and far-field as shown in Figure 2.1. The transition is gradual between the regions and there are no distinct boundaries.

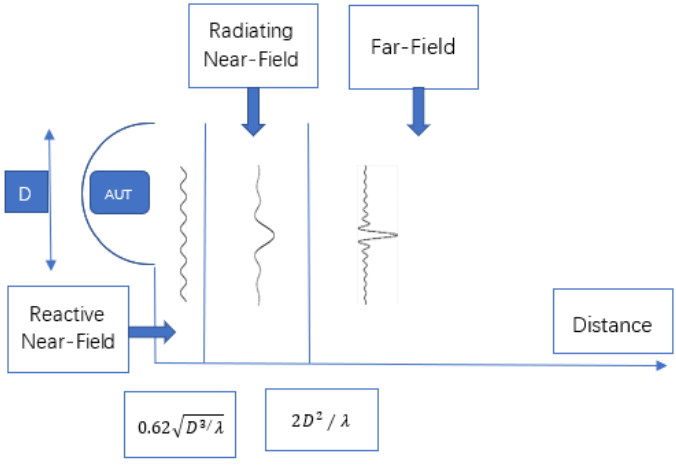

Figure 2.1: Antenna Field Regions [4]

Reactive near-field region: The portion of the region surrounding the antenna, where the reactive fields predominate [7]. It starts from the surface of the antenna and ends usually at $0.62\sqrt{(D^3/\lambda)}$ where λ is the wavelength and D is the largest dimension of the antenna.

Radiating near-field region: It is also known as the Fresnel region, it is an intermediate region, where the radiation fields predominate, and the angular field distribution depends on the distance from the antenna. It starts at $0.62\sqrt{D^3/\lambda}$ and ends usually at $2D^2/\lambda$ from the antenna.

Far-field: It is also known as the Fraunhofer region, it starts from $2D^2/\lambda$ to infinity and the angular field, distribution does not depend on the distance from the antenna.

2.2 Near-field vs Far-field

The near-field or far-field technique is used based on significant cost, size, complexity, and architecture of the antenna. The major features of both techniques are listed in Table 2.1.

Table 2.1: Near-field vs Far-field

Near-Field Techniques	**Far-Field Techniques**
Measurement indoors - Controlled environment - Facility size comparable to Antenna under test (AUT) size.	Measurement outdoors - Reflections, RF interference, weather uncertainties. Measurement indoors - Controlled environment - AUT size limitation
NFTFF transformation is necessary - The field is calculated everywhere - Significantly more data are required - Precise alignment is required - Long measurement time	Far-field is measured directly - Only necessary data are measured - Short measurement time
Highest accuracy is achievable	Moderate accuracy is achievable

The near-field measurement technique is well suited for different types of antennas like:

- Millimeter-wave antennas (high atmospheric loss)
- Adjustment of array antennas/scanning antennas
- Non-reciprocal antennas
- Shaped beam and low side-lobe antennas.

2.3 Huygens equivalence principle

The Huygens equivalence principle is one of the fundamental concepts in electromagnetics and widely used. In this theorem, the actual sources are substituted by equivalent sources and the equivalent sources generate the same fields as the actual sources in the region of interest [6].

Let's consider a surface S, the field outside the surface is obtained by substituting equivalent electric and magnetic current over the surface as shown in Figure 2.2.a. The actual radiating source is J_s, M_s and radiating fields E_1, H_1, and n is a unit normal vector pointing outward. An equivalent radiating source can be substituted by surface electric and magnetic current (Love's equivalence principle) as shown in Figure 2.2.b. Similarly, surface magnetic current with PEC filled inside as shown in Figure 2.2.c or electric current with PMC filled inside as shown in figure 2.2.d can be substituted as an equivalent radiating source.

The Huygens equivalence principle provides the theoretical basis for near-field measurements [6]. The near-field measured data is used to determine equivalent electric and magnetic current sources over the imaginary Huygens surface which surrounds the antenna. The near-field to far-field (NFTFF) transformation is performed using the equivalence principle to predict the far-field.

Huygens principle requires a closed surface, a planar scanning surface is not closed. Another approach would be a very large near-field scanning surface for accurate far-field estimation as shown in paper [8] and it may be unrealistic, time-consuming, and cost-ineffective.

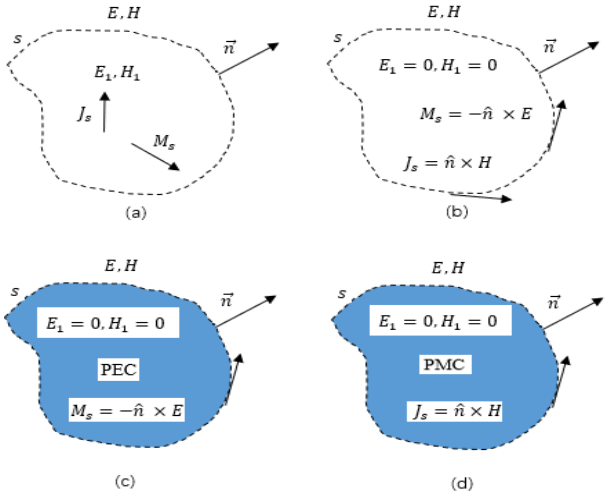

Figure 2.2: Equivalence principle models[7].

2.4 Plane waves

A plane wave is a constant-frequency wave whose wavefronts are infinite parallel planes of constant peak-to-peak amplitude normal to the phase velocity vector. An antenna produces a field that is locally approximately a plane wave in its far-field region. If in the region of the antenna a plane wave can be produced by means other than the far-field source, the far-field response can be measured equally well.

In free space, electromagnetic wave propagation is treated as the expansion of many patterns of a wave. In a source-free, linear, homogeneous region, wave propagation is modelled by Maxwell equations [6] and can be transformed into following Helmholtz vector wave equations:

$$\nabla^2\mathbf{E} + \mathrm{k}^2\mathbf{E} = 0 \tag{2.1}$$

$$\nabla^2\mathbf{H} + \mathrm{k}^2\mathbf{H} = 0 \tag{2.2}$$

Here k is the wavenumber and a vector show the propagation direction. A wave can be defined in terms of the same frequency plane waves propagating in different directions having different amplitudes.

$$\mathbf{E}(\mathrm{x},\mathrm{y},\mathrm{z}) = \frac{1}{4\pi^2}\int_{-\infty}^{\infty}\int_{-\infty}^{\infty}\mathbf{A}(\mathrm{k_x},\mathrm{k_y})\mathrm{e}^{-\mathrm{j}\mathbf{k}\cdot\mathbf{r}}\mathrm{d}\mathrm{k_x}\,\mathrm{d}\mathrm{k_y} \tag{2.4}$$

$$\mathbf{H}(\mathrm{x},\mathrm{y},\mathrm{z}) = \frac{1}{4\pi^2}\int_{-\infty}^{\infty}\int_{-\infty}^{\infty}\mathbf{k} * \mathbf{A}(\mathrm{k_x},\mathrm{k_y})\mathrm{e}^{-\mathrm{j}\mathbf{k}\cdot\mathbf{r}}\mathrm{d}\mathrm{k_x}\,\mathrm{d}\mathrm{k_y} \tag{2.5}$$

$\mathbf{A}(\mathrm{k_x},\mathrm{k_y})$ here is the plane wave spectrum function. From eqn [2.4] and eqn [2.5], the electromagnetic field in free space can be regarded as a sum of plane waves

propagated in different angles. If the vector magnitude of a plane wave is received, the vector magnitude of the electric field and magnetic field can be obtained by Fourier transform.

In the near-field measurements, the measured complex near-field data is converted through the two-dimensional Fourier transforms into plane waves in the k-space. The objective of plane wave expansion is to determine the amplitudes and the directions of the plane waves. The far-field pattern of the antenna will be obtained in terms of the PWS(plane waves spectrum) function.

3

Design and Implementation

The near-field antenna measurement was started probably by Barrett and Barnes [9] in the 1950s. Later, activities in near-field measurements were increasing beginning with the probe correction technique proposed by Kerns [9], [10]. A comprehensive review of near-field measurements and its development was given Yaghjian [12], beginning with ideal probes scanning on arbitrary surfaces and ending with scanning on planar, cylindrical, and spherical surfaces. An advent of the Fast Fourier Transform (FFT) technique, as well as rapid progress in electronics, signal processing made near-field measurements fast, accurate, and economical. In this chapter a brief description of system design, algorithms used and implementation.

3.1 Design overview

The top-level flow as shown in Figure 3.1 is used in designing the near-field measurement system and implemented. The scanning is made in a specific pattern, scan area is controlled by sampling values. The near-field data are collected at the specific points based on the sampling values by the probe in the specified scanning pattern. The measured near-field data is processed in MATLAB using the PWS method by Fourier transforms and the far-field pattern E-plane and H-plane are obtained. [7]

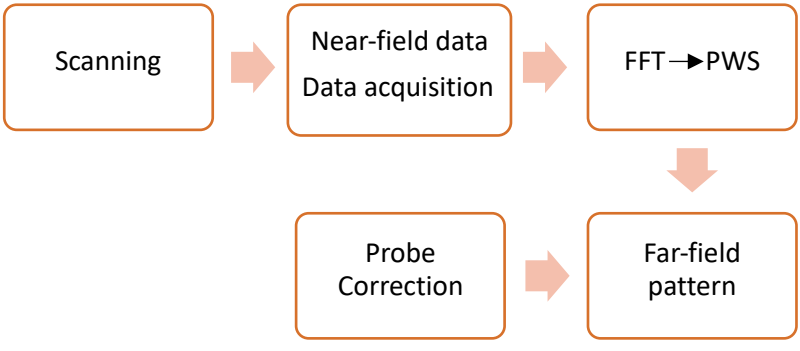

Figure 3.1: Design Overview

3.2 Antenna under test

The standard gain horn antenna of 20 dB gain with frequency range 26.5 GHz-40 GHz is provided by the company as in Figure 3.2 and details are presented in Table 3.1.

The horn antenna is used as the AUT, since the horn is among the simplest, enables matching the impedance of the waveguide to that of free space or vice versa, helps suppress signals traveling via unwanted modes in the waveguide from being radiated and it provides a significant level of gain and directivity [12]. It has a very wide bandwidth; its performance varies little over a wide frequency range.

Table 3.1: Horn antenna specifications

Frequency (GHz)	26.5 – 40.0
Waveguide type	WR28
Gain (dB)	20
Polarization	Linear
Size (mm)	32.1 x 40.4 X 94
Material	Copper

Figure 3.2: WR28 standard gain horn antenna

3.3 Probe

The selection of the probe depends on several factors. The desired properties for near-field antenna measurement probes are often contradictory and cannot be fully achieved. Some of the important features are:

- To minimize impedance mismatch and reduce multiple reflections, the return loss of the probe should be at least 10 dB.
- The probe shouldn't have any nulls in its pattern as the uncertainty will be large in that direction.
- Wide bandwidth and easy to handle
- To minimize multiple reflections between probe and AUT, the probe's effective area must be small, and this means lesser gain. But too large indifference in gain between AUT and probe results in a high insertion loss and will result in a less accurate measure of AUT gain and pattern [14]. The probe with gain approximately 10-20 dB less than the AUT is recommended.

The open-ended rectangular waveguide (OERWG) is commonly used as a probe in near-field measurements. The influence of geometrical parameters on the measured field is done in [15] for OERWG and horn antenna. The results show that OERWG measured fields are higher and better than horn antenna for AUT far-field pattern prediction. Also, in [16] measured fields for different aperture sizes of horn and OERWG, results showed that OERWG is the better option.

Based on the study from the relevant papers on probes [14], we ordered a WR28 rectangular straight waveguide and WR28 waveguide to the coaxial adapter as a cost-effective solution for a probe as shown in Figure 3.3 and specifications are presented in table 3.2.

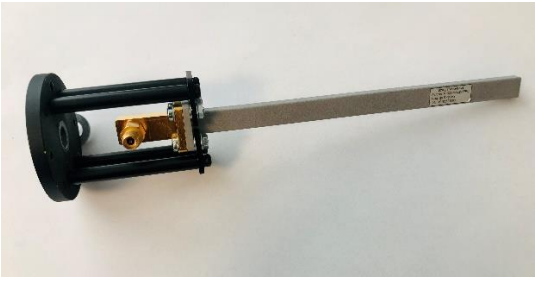

Figure 3.3: Waveguide with coaxial adapter

Table 3.2: Waveguide specifications

Waveguide type	WR28
Frequency range	26.5 – 40 GHz
Connector	2.92 mm female
Size	7.112 x 3.556 x 150 mm
Material	Copper

Based on the specifications, the waveguide was designed in the HFSS tool to determine the effects of various parameters on its performance. The simulations were done for a frequency range of 26 GHz – 42 GHz and for different lengths of the waveguide 100 mm – 250 mm. The gain of the waveguide for different frequencies and lengths are as shown in Figure 3.4. The gain of the waveguide increases with the frequency and the variation of the length does not affect much to gain the probe, means that length is negligible. The S11 of the waveguide for different frequencies and lengths are as shown in Figure 3.5, there was a unnormal point at 30GHz may cause by software sampling error, and we are not interested at this frequency so just ignored it. The S11 of the waveguide increases with the frequency and a maximum of 0.3 dB difference was observed in S11 of the probe with the variation of length of the probe.

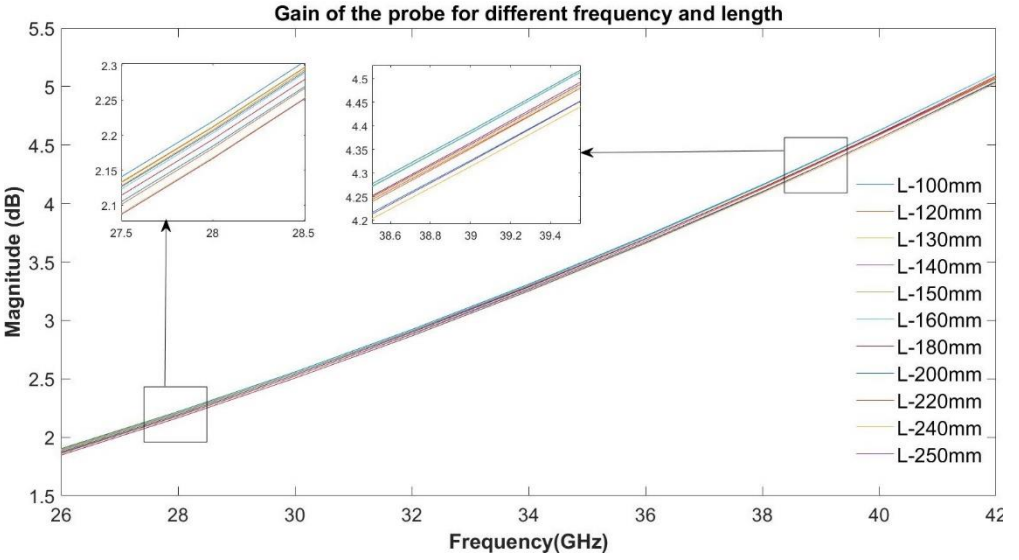

Figure 3.4: Gain of the probe for different frequency and length of the probe

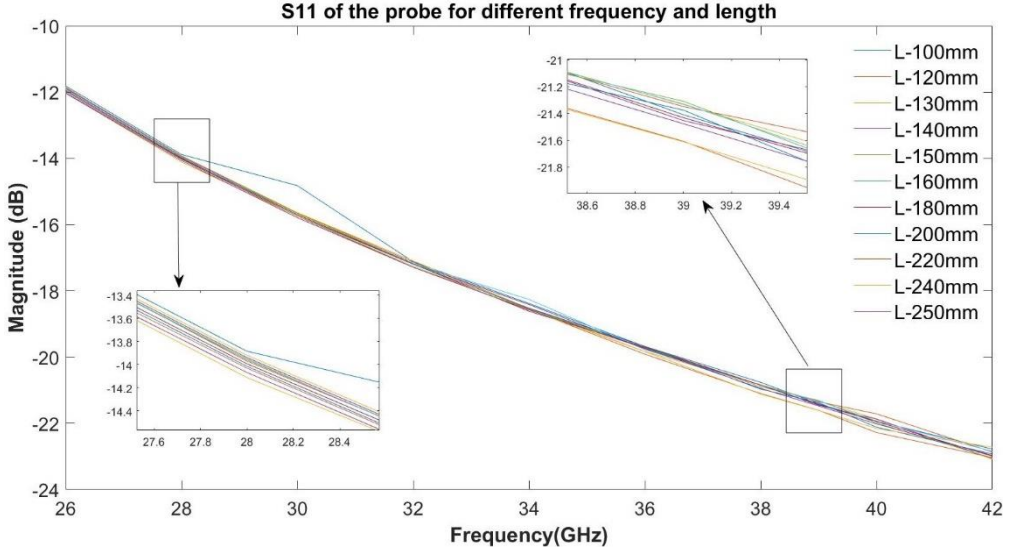

Figure 3.5: S11 of the probe for different frequency and length of the probe

The probes are sensitive to the tangential component of the electric field and to normal components due to the interaction of the field lines with the external conductor of the excitation probe, which creates uncertainty on the measures. To overcome this

a ground plane reflector is added to have a better rejection ratio of the normal component. The effect was studied by the designed probe without a metallic plane and various sizes of planes for frequency 28 GHz and 39 GHz. The voltage at the output of the probe for different sizes of the plane is as shown in Figure 3.6 and Figure 3.7. It was observed that the rate of rejection of the normal component of the field increased with an increase in the size of the metallic plane. Alternatively, increase the size of the metallic plane disturbs the propagation mode of the guide resulting from coupling with the metallic plane. For this reason, the dimensions of this plane reflector are optimized by the method of finite integrals by varying its section in such a way that the new probe disturbs less the measurements and the electromagnetic behaviour of the AUT.

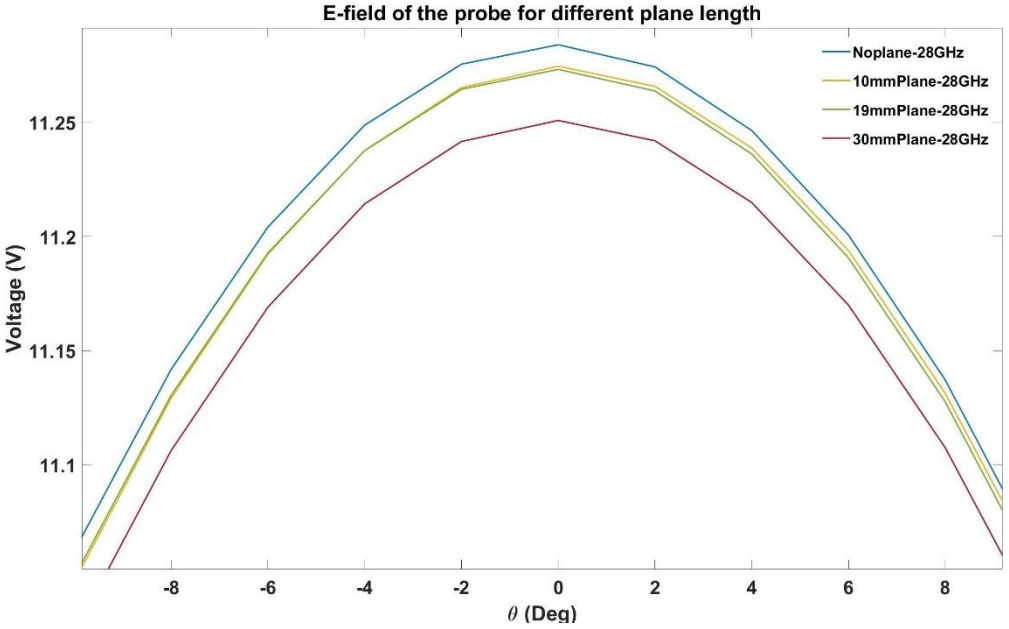

Figure 3.6: E-field of the probe for different size of the plane for 28GHz

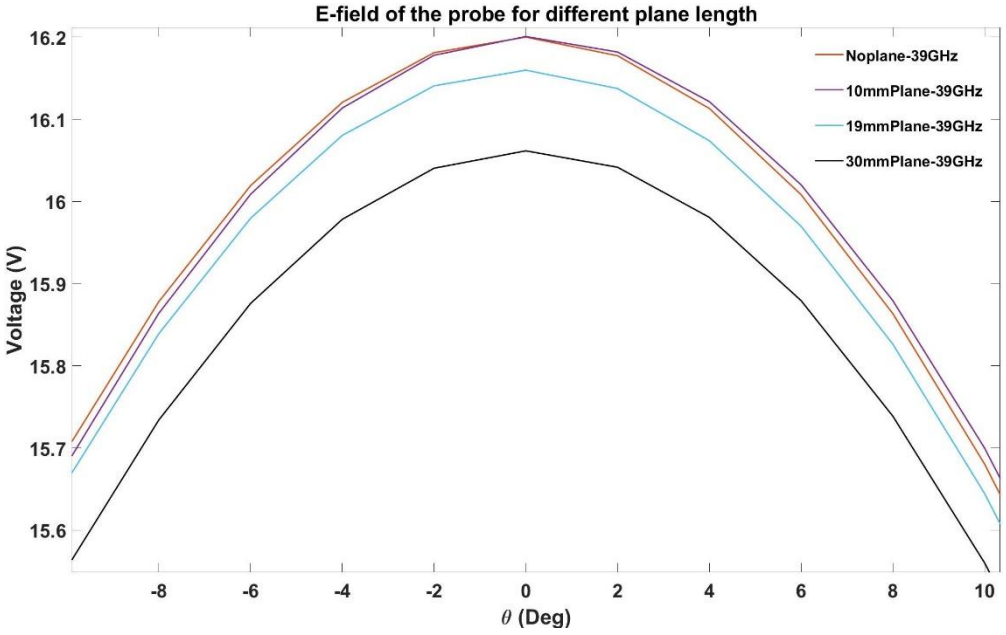

Figure 3.7: E-field of the probe for different size of the plane for 39GHz

3.4 Separation distance

The far-field pattern varies with the separation distance between the AUT and probe, several factors must be considered for choosing a separation distance [14]. Few necessary factors are:

- A minimum separation of 3 λ-5 λ is necessary to avoid evanescent (non-propagating) modes contributing to the measured near-field data, since the probe response at these modes is difficult to determine.
- As the separation distance increases, the valid region of the pattern decreases for a given scan area.
- As the separation distance decreases the multiple reflections between AUT and probe increase. Hence a separation distance must be counterbalanced between pattern coverage and multiple reflections for a better far-field pattern.

Based on the dimensions of AUT, the separation distance is calculated for different frequencies and presented in Table 3.3. The near-field region of the AUT starts from $0.62\sqrt{D^3/\lambda}$ and far-field starts from $2D^2/\lambda$, where D is the largest dimension of

AUT and λ is the wavelength. So, the separation distance must be within the near-field range at least $0.62\sqrt{D^3/\lambda}$.

Table 3.3: Separation distance based on the frequency

Frequency (GHz)	Near-field (mm)	Far-field (mm)	Separation distance (mm)
28	48.65	304.79	~ 49-300
39	57.37	423.93	~ 58-420

3.5 Scanner

The near-filed measured data is acquired by using a probe to scan the field over a preselected geometrical surface, which may be a plane, a cylinder, or a sphere. The fundamental limitations and inherent advantages of each configuration should be considered for selecting the surface.

3.5.1 Scanning geometrics

Planar: In planar scanning, the AUT is stationary and the probe moves along a planar surface in X and Y directions in steps of Δx, Δy, and near-field data is gathered at specific X, Y locations as shown in Figure 3.8. The planner scanning is mostly used for highly directive antennas where nearly all the transmitted or received energy passes through the planar scan area. It requires the least amount of computations and alignment compared to other methods.

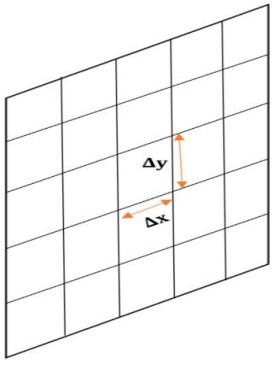

Figure 3.8: Planar Scanning

Cylindrical: In cylindrical scanning, the AUT is mounted on a rotator in Ø coordinate and the probe move on the cylindrical surface at various heights in Δz steps as shown in Figure 3.9 and a grid of samples are taken along the azimuth and z. Due to the truncation of the scanning aperture in the z-direction, a limited elevation pattern is obtained. This method is useful in cell phone base station antennas where the energy is directional in one axis and broad in the orthogonal axis.

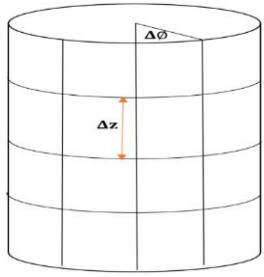

Figure 3.9: Cylindrical Scanning

Spherical: In spherical scanning, the probe is stationary and the AUT is mounted on a dual-axis rotator that positions θ axis, and Ø axis. An alternative is to keep AUT rotated around the z-axis in ΔØ steps and the probe is moved in circular in Δθ steps as shown in Figure 3.10 and a grid of samples is taken at each step. The advantage of this method is AUT three-dimensional pattern can be obtained and suitable for any antenna. The primary drawback is the mechanism accuracy.

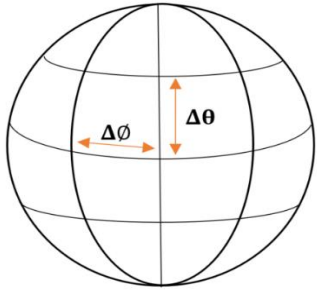

Figure 3.10: Spherical Scanning

3.5.2 Designed Scanner

The planar scanner is designed, as it is easier to implement, data processing is simpler and usually suitable for antennas of high directivity. To reduce the cost and time, the existing scanner in the company was used as shown in Figure 3.11 The scanner moves in X, Y direction with scan area 165 cm * 175 cm. The movement of a scanner is done using two stepper motors (NEMA 17), they are controlled by Arduino Uno and Aadafruit motor shield.

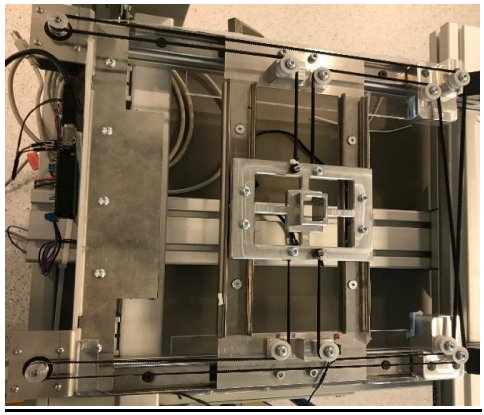

Figure 3.11: Designed Scanner

Stepper motor: A stepper motor is a brushless, synchronous electric motor that converts digital pulses into mechanical movement of the shaft. Stepper motors operate in discrete steps, they have several coils in groups called phases [18]. The motor will rotate one step at a time by energizing each phase in a sequence. The number of steps per revolution is given by a complete 360° circle divided by the step angle.

A NEMA17 stepper motor is used in the design as in Figure 3.12 Its rated voltage is 5v, holding torque is 49 N/cm, step angle of 1.8° with 200 steps per revolution.

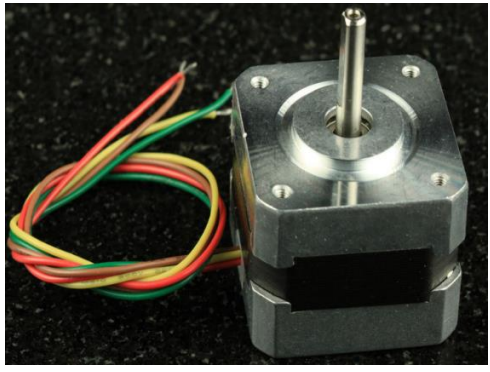

Figure 3.12: Stepper motor NEMA17 [16]

Arduino Uno: It is a microcontroller board based on the ATmega328P as in Figure 3.13, it has 14 digital I/O pins (of which 6 can be used as pulse width modulation outputs), 6 anal og inputs, a 16 MHz quartz crystal and Arduino software IDE (Integrated development environment) which allows to write programs and upload to board [18]. The stepper can be controlled in the required steps and direction by Arduino Uno.

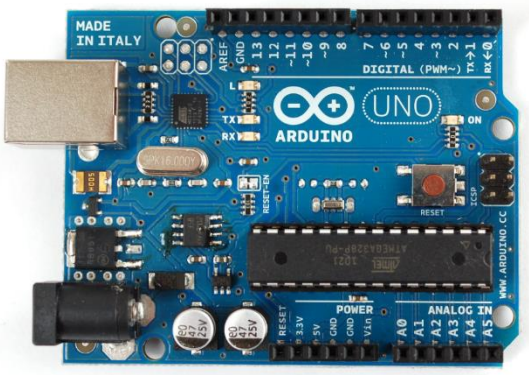

Figure 3.13: Arduino UNO [16]

Adafruit motor shield: Driving a stepper motor is a bit more complicated than driving a regular DC motor. Stepper motors require a stepper controller to energize the phases in a timely sequence to make the motor run [18]. The controller module (Arduino in our case) will not be able to provide enough current from its I/O pins for the motor to rotate. So, an external module like the Adafruit motor shield module as a stepper motor driver is used in the design as in Figure 3.14 it can drive up to two stepper motors. The driver chips are interfaced via a dedicated PWM driver chip with an I2C interface.

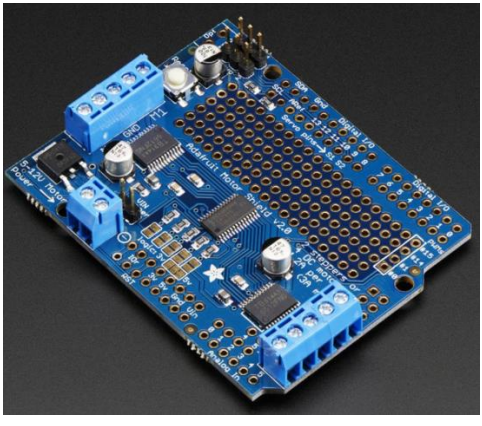

Figure 3.14: Adafruit motor shield [16]

It requires 1714 x 1908 steps for a stepper motor to cover the scan area of 165 mm x 175 mm. A code was developed in Arduino IDE to control the steps, speed, and direction and uploaded it to the board. An interface was created using python to control the scan area based on the required step size and the scan length. Based on the inputs, the scanner adjusts and starts scanning in a specific pattern as in Figure 3.15.

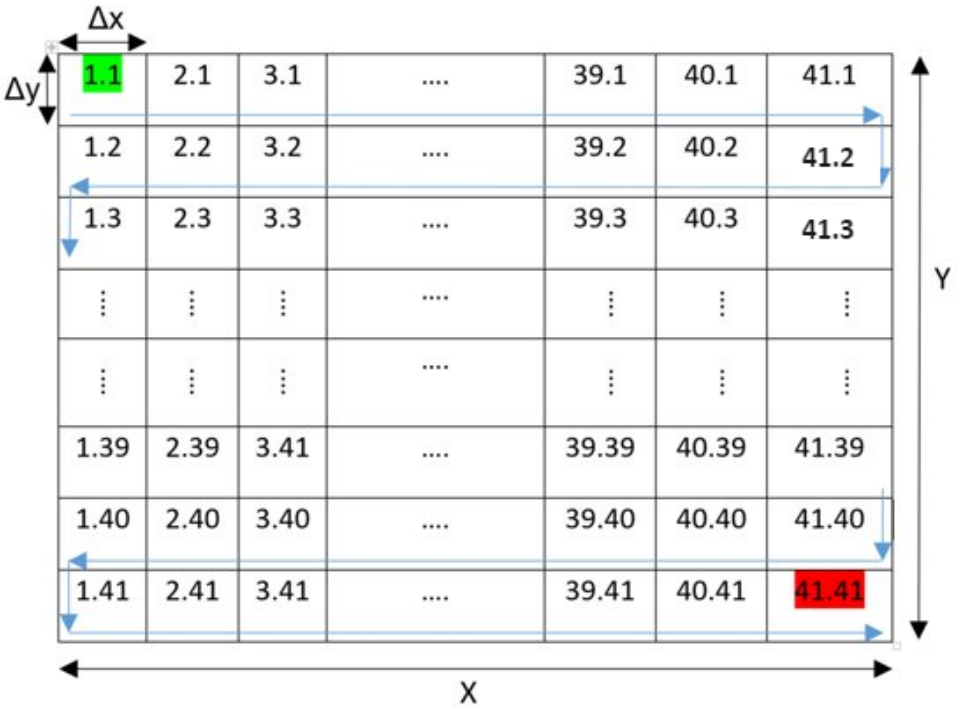

Figure 3.15: The Planar of the Scanner and the scanning movement. Numbers indicates the coordinates in the scanning plane. Green is the starting point, and red is the end point.

3.5.3 Sampling and scan area truncation

The sampling points on the measuring grid is better chosen less than $\lambda/2$ in order to satisfy Nyquist sampling criteria to avoid aliasing i.e. $\Delta x = \Delta y \leq \lambda/2$ but not requirement. The size of the scan area must be large enough to accept all significant energy from the AUT. The calculated far-field pattern of AUT will be valid in the region between $\pm\theta$ [16] as sown in Figure 3.16.

$$\theta_{\pm} = \arctan\left(\frac{L_{\pm} - \frac{D}{2}}{z}\right) \quad (3.1)$$

Where,

$L_{\pm}$ is the length of that portion of the scan above(below) the z-axis

D is the AUT diameter

z is the separation distance between AUT and the scan plane

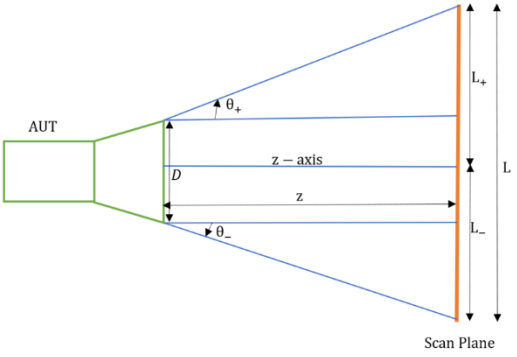

Figure 3.16: Scan area truncation [17]

The valid angle is calculated from (3.1) for the scan area length L=165 mm, the AUT diameter a=40.4 mm and the separation distance varies for different frequencies and the valid angle of far-field that can be achieved with this configuration as shown in Table 3.4.

Table 3.4: The valid angle of far-field data

Frequency (GHz)	**Separation distance (mm)**	**Valid angle (Deg)**
28	50 (min)	51.25
	300 (max)	11.73
39	60 (min)	46.07
	420 (max)	8.43

3.6 Near-field data

The planar near-field measurement requires a signal source, receive system, scanner, AUT and probe. The measurement system is illustrated in Figure 3.17. The near-field measurements are done in an anechoic chamber where the absorbers are placed on the walls to avoid reflections and reduce the effects of stray signals. The anechoic chamber was designed with the dimensions 68 cm x 73 cm x 165 cm. The Keysight PNA N5227B vector network analyzer (VNA) is used to generate the source signal and serves as the receiver. The VNA and the computer are connected through the GPIB-USB interface. The cable and connector type need to support the frequency range of the measurements and are calibrated to compensate for the losses.

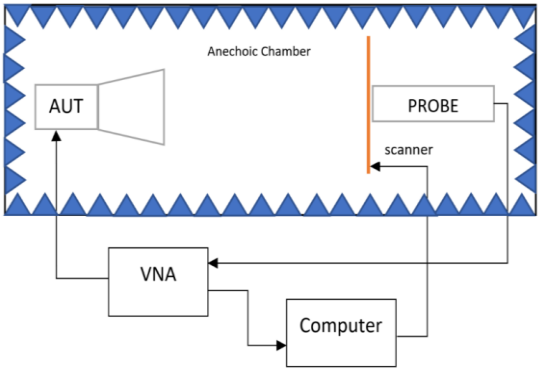

Figure 3.17: Measurement system

Vector network analyzer: The VNA measures the transmitted and reflected waves as a signal through a device under test [19]. It measures both the amplitude and phase of the signal. Usually, VNA is used to measure the S-parameters.

GPIB: General purpose interface bus or IEEE 488 bus is one of the more popular and versatile interfaces which allows data to flow between any of the instruments on the bus, at a speed suitable for the slowest active instrument [19]. The National Instruments GPIB-USB-HS as in Figure 3.18 is used, it transforms any computer with a USB port into a full-function and can control the instruments.

Figure 3.18: National Instruments GPIB-USB-HS [17]

The AUT and probe are aligned so that their coordinate system is parallel. The probe x and y axes are aligned parallel to the scanner x and y axes. The scanner area is adjusted based on the step size and scan length, and the S21 (amplitude and phase) data are collected from the probe at each location as in Figure 3.19 by VNA and measured near-field data are stored in excel sheet in the local computer. The OERWG probe measures only one polarization, but the far-field pattern requires near-field data in both polarizations, vertical and horizontal. Hence, the probe is rotated by 90° to receive both polarizations. So, every measurement is conducted for both polarizations separately.

```
Automatic probing Started
------------------------------

c:\users\erfhlab\appdata\local\programs\python\python37-32\lib\site-
packages\pyvisa\resources\messagebased.py:590: FutureWarning: query_values is deprecated and
will be removed in 1.10, use query_ascii_values or quey_binary_values instead.
  'instead.', FutureWarning)
11:18:34 --> Saved results for coordinates:(1,1) --> steps (17,1794)
11:18:36 --> Saved results for coordinates:(2,1) --> steps (58,1794)
11:18:38 --> Saved results for coordinates:(3,1) --> steps (99,1794)
11:18:40 --> Saved results for coordinates:(4,1) --> steps (140,1794)
11:18:43 --> Saved results for coordinates:(5,1) --> steps (181,1794)
11:18:45 --> Saved results for coordinates:(6,1) --> steps (222,1794)
11:18:47 --> Saved results for coordinates:(7,1) --> steps (263,1794)
11:18:49 --> Saved results for coordinates:(8,1) --> steps (304,1794)
11:18:52 --> Saved results for coordinates:(9,1) --> steps (345,1794)
11:18:54 --> Saved results for coordinates:(10,1) --> steps (386,1794)
```

Figure 3.19: Measured data at each location

3.7 Near-field to far-field transformation

Our near-field to far-field transformation is done based on plane wave spectrum expansion. The measured near-field data is converted to plane waves in the k-space by means of the two-dimensional Fourier transforms in MATLAB.

An electromagnetic field in space can be expressed by a series of a plane wave, which spreads over different directions. Thus, the electric field can be represented [7] by

$$\mathbf{E}(x,y,z)=\frac{1}{4\pi^2}\int_{-\infty}^{\infty}\int_{-\infty}^{\infty}\vec{A}(k_x,k_y)e^{-j\,\vec{k}\cdot\vec{r}}dk_x dk_y \tag{3.2}$$

Where

$$\vec{A}(k_x,k_y)=A_x(k_x,k_y)\hat{\mathbf{x}}+A_y(k_x,k_y)\hat{\mathbf{y}}+A_z(k_x,k_y)\hat{\mathbf{z}} \tag{3.3}$$

$$\vec{k}=k_x\hat{\mathbf{x}}+k_y\hat{\mathbf{y}}+k_z\hat{\mathbf{z}} \tag{3.4}$$

$$\vec{r}=x\hat{\mathbf{x}}+y\hat{\mathbf{y}}+z\hat{\mathbf{z}} \tag{3.5}$$

Where k_x,k_y and k_z are wavenumbers in x, y respective z-direction.

In (3.2) , $\vec{A}$ is called the plane wave spectrum because of the expression $\vec{A}(k_x,k_y)e^{-j\,\vec{k}\cdot\vec{r}}$ in the integrands represents a uniform plane wave propagating in the direction of k.

To get the far field pattern from near field measurement at least we need 3 steps:

1. Get the electric field components $E_x(x,y,z=0)$ and $E_y(x,y,z=0)$
2. Find the plane wave spectrum $A(k_x,k_y)$.
3. Determine the far field.

The measured near-field x and y component of the electric field over a plane surface (z =0) from equation 3.2 is given by

$$E_x(x,y,0)=\frac{1}{4\pi^2}\int_{-\infty}^{\infty}\int_{-\infty}^{\infty}A_x(k_x,k_y)e^{-j(k_x x+k_y y)}\,dk_x dk_y \tag{3.6}$$

$$E_y(x,y,0)=\frac{1}{4\pi^2}\int_{-\infty}^{\infty}\int_{-\infty}^{\infty}A_y(k_x,k_y)e^{-j(k_x x+k_y y)}\,dk_x dk_y \tag{3.7}$$

Where $(k_x x+k_y y)$ represent $\vec{k}\cdot\vec{r}$ in coordinate system.

The near-field measurements over the plane surface are divided into a grid of M x N points spaced Δx and Δy apart and defined by coordinates ($m\Delta x, n\Delta y,0$). The values of M and N are determined by the linear dimensions of the sampling plane divided by the sampling space.

$$M=\frac{a}{\Delta x}+1 \tag{3.8}$$

$$N=\frac{b}{\Delta y}+1 \tag{3.9}$$

Where a and b are the width and height of the scan area.

The far-field pattern requires both polarization components since the probe used is linearly polarized the probe is rotated by 90° to obtain the other polarization. The tangential electric field components E_x and E_y the two polarizations of the probe are obtained at the grid sample points and are reconstructed over the entire plane and each is given. So, the all-electric field components function is:

$$E_x(x,y,z=0)\cong \sum_{n=-\frac{N}{2}}^{\frac{N}{2}-1}\sum_{m=-\frac{M}{2}}^{\frac{M}{2}-1} E_x(m\Delta x, n\Delta y ,0)* \frac{\mathrm{Sin}(K_{x0}x-m\pi)}{(K_{x0}x-m\pi)}\ \frac{\mathrm{Sin}(K_{x0}y-n\pi)}{(K_{x0}y-n\pi)} \tag{3.10}$$

$$E_y(x,y,z=0)\cong \sum_{n=-\frac{N}{2}}^{\frac{N}{2}-1}\sum_{m=-\frac{M}{2}}^{\frac{M}{2}-1} E_y(m\Delta x, n\Delta y ,0)* \frac{\mathrm{Sin}(K_{x0}x-m\pi)}{(K_{x0}x-m\pi)}\ \frac{\mathrm{Sin}(K_{x0}y-n\pi)}{(K_{x0}y-n\pi)} \tag{3.11}$$

So (3.10) is the sum of all the measurement electric field components by different place in the planar scanning. The Sin function inside is to get the tangential electric value of different place. And (3.11) is the same but after rotating probe 90° to get the other polarization.
Then Using (3.10) and (3.11) to get the plane wave spectrum, A_x and A_y of (3.12) and (3.13) can be evaluated using an IFFT algorithm and given by

$$A_x(k_x,k_y)=\int_{-\frac{b}{2}}^{+\frac{b}{2}}\int_{-\frac{a}{2}}^{+\frac{a}{2}} E_x(x,y,z=0)e^{+j(k_xx+k_yy)}\,dxdy \tag{3.12}$$

$$A_y(k_x,k_y)=\int_{-\frac{b}{2}}^{+\frac{b}{2}}\int_{-\frac{a}{2}}^{+\frac{a}{2}} E_y(x,y,z=0)e^{+j(k_x x+k_y y)}\,dxdy \tag{3.13}$$

Where a, b are width and height of the scan area.
And k_x,k_y and k_z are wavenumbers in x, y respective z-direction and can be written as a function of angles and in a spherical coordinate system.

$$k_x=k\sin\theta\cos\phi \tag{3.14}$$

$$k_y=k\sin\theta\sin\phi \tag{3.15}$$

$$k_z=k\cos\theta \tag{3.16}$$

The far-field pattern of the antenna in a plane-wave spectrum function is hard to calculated by using stationary phase method to get the approximate far field pattern is as follows [7]:

$$\vec{E}(r,\theta,\emptyset)\cong j\frac{ke^{-jkr}}{2\pi r}[\cos\theta\,\vec{A}(k_x,k_y)] \tag{3.17}$$

Or the field can be reprented by spherical coordinate below:

$$E_\theta(r,\theta,\emptyset)\cong j\,\frac{ke^{-jkr}}{2\pi r}\left(A_x\cos\emptyset+A_y\sin\emptyset\right) \tag{3.18}$$

$$E_\emptyset(r,\theta,\emptyset)\cong j\frac{ke^{-jkr}}{2\pi r}\cos\theta\left(-A_x\sin\emptyset+A_y\cos\emptyset\right) \tag{3.19}$$

3.8 Probe correction

The probe's far-field pattern differs appreciably from the far-field of an elementary electric and magnetic dipole [20]. Thus, it is required to correct the nonideal receiving response of the probe for the accurate determination of electric and magnetic fields from near-field measurements. In planar scanning, the probe remains oriented in the same direction and the sidelobe field is sampled at an angle off the boresight direction of the probe [11]. Hence, the probe correction is required for planar near-field measurements which compensates for this off-boresight sampling by the nonideal probe of the plane waves radiated by the AUT.

By the Lorentz Reciprocity theorem, we can obtain the coupling equation between AUT and the probe, then can derive the probe compensation equations [21]. Let the AUT be in the region of $z<0$, s_0 and s' is the reference transverse section in the feed

line of AUT and the probe respectively as in Figure 3.20. The distance between AUT and the scanning plane is d, $\overrightarrow{r_0}$ is the position vector of the probe $\overrightarrow{r_0}=(x',y',z')$. The received power of probe is given by [21]

$$P_r(x,y,d)=\frac{8\pi^2}{\omega\mu}\int_{-\infty}^{+\infty}\int_{-\infty}^{+\infty} k_z A(\vec{k})*\vec{B}(\vec{k}')e^{(-j\vec{k}\cdot\overrightarrow{r_0})}\ dk_x dk_y \tag{3.20}$$

Where

$k_z=\sqrt{k^2-k_x^2-k_y^2}$

$\vec{A}(\vec{k})$ is AUT EM field spectrum (in $o-xyz$ coordinate)

$\vec{B}(\vec{k}')$ is probe EM field spectrum (in $o'-x'y'z'$ coordinate)

$\overrightarrow{r_0}=x\hat{x}+y\hat{y}+z\hat{z}$

In equation (3.20) we can easily know that $k_z\vec{B}(\vec{k}')$ is proportional to the probe patterns. When plane wave $\vec{A}(\vec{k})\exp(-j\vec{k}\cdot\overrightarrow{r_0})$ radiated to the probe, the probe's transmitting power is proportional to $\vec{A}(\vec{k})\exp(-j\vec{k}\cdot\overrightarrow{r_0})k_z\vec{B}(\vec{k}')$. So integral all the responses of planewaves from different direction probe received with k_x, k_y, we can get the AUT's transmitting signal.

When $k_x^2+k_y^2>k^2$, so the plane wave's EM spectrum alone z axis is logarithm attenuated. So usually the d (distance between probed and AUT) in near-field measurement is much more than several wavelengths. In this case, when the attenuated wave reaches the scanning plane is too low to measure. So practically, we only consider $k_x^2+k_y^2<k^2$, means $|k_x|<k$, $|k_y|<k$.

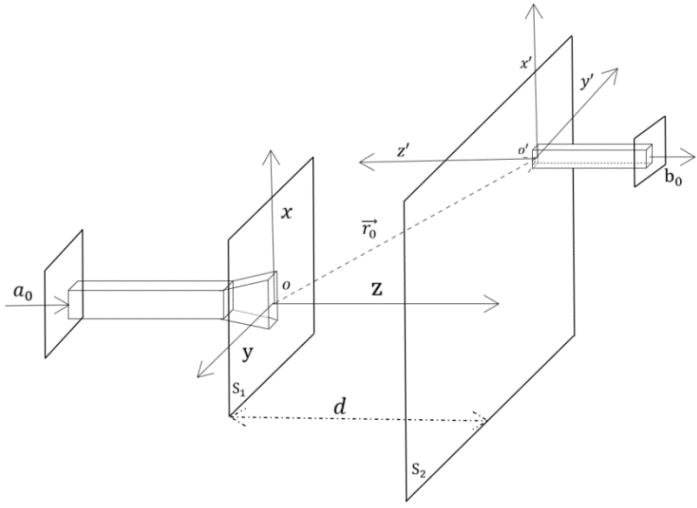

Figure 3.20: Planar near-field measurement illustration

The relation of plane wave EM spectrum to the patterns:

$\vec{F}(\vec{k}) = C_1 k_z \vec{A}(\vec{k})$ and $\vec{F}(\vec{k}) = C_2 k_z \vec{B}\left(\overrightarrow{k'}\right)$

Where C_1, C_2 are constants

$\vec{F}(\vec{k})$ is the AUT's far field pattern.

$\overrightarrow{F'}\left(\overrightarrow{k'}\right)$ is the probe's far field pattern.

So, we can simplify equation 3.20 into:

$$P_r(x,y,d) = C \iint_{k_x^2+k_y^2<k^2} \frac{\vec{F}(\vec{k})\cdot\vec{F}(\vec{k})\exp(-j\vec{k}\cdot\overrightarrow{r_0})}{k_z} dk_x dk_y \quad (3.21)$$

Where C is constant

In figure 3.21,

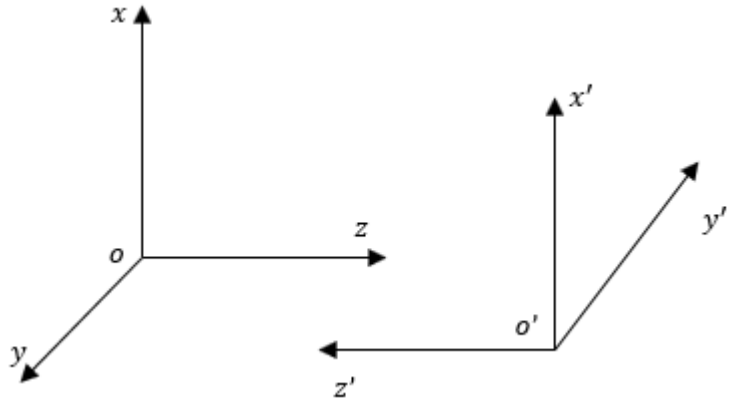

Figure 3.21: Coordinator System of the first measurement

$\hat{x} = \widehat{x'}, \hat{y} = \widehat{y'}, \hat{z} = -\widehat{z'}$

$\theta = \theta', \phi = \pi - \phi'$ (3.22)

Use equations above and transformation of between spherical coordinate system to Cartesian coordinate system, can obtain:

$$\begin{aligned}\widehat{\theta'} &= cos\theta' cos\phi' \widehat{x'} + cos\theta' sin\phi' \widehat{y'} - sin\theta' \widehat{z'} \\ &= - cos\theta cos\phi \hat{x} - cos\theta sin\phi \hat{y} + sin\theta \hat{z} \\ &= -\hat{\theta}\end{aligned} \quad (3.23)$$

$$\begin{aligned}\widehat{\phi'} &= - sin\phi' \widehat{x'} + cos\phi' \widehat{y'} \\ &= - sin\phi \hat{x} + cos\phi \hat{y} \\ &= \hat{\phi}\end{aligned} \quad (3.24)$$

$$\begin{aligned}\overrightarrow{k'} &= k_0(sin\theta' cos\phi' \widehat{x'} + sin\theta' sin\phi' \widehat{y'} + cos\theta' \widehat{z'}) \\ &= -k_0(sin\theta cos\phi \hat{x} + sin\theta sin\phi) \\ &= -\vec{k}\end{aligned} \quad (3.25)$$

Next, represent the AUT and the probe far field patterns as below:

$\vec{F}(\theta, \phi) = f_\theta(\theta, \phi)\hat{\theta} + f_\phi(\theta, \phi)\,\hat{\phi}$ (3.26)

$\overrightarrow{F'}(\theta', \phi') = f'_{\theta'}(\theta', \phi')\widehat{\theta'} + f'_{\phi'}(\theta', \phi')\,\widehat{\phi'}$ (3.27)

Use equations3.23,3.24,3.25 can elevate equation 3.27

$\vec{F}(\theta, \phi) = -f'_{\theta'}(\theta', \pi - \phi)\hat{\theta} + f'_{\phi}(\theta, \pi - \phi)\hat{\phi}$ (3.28)

Define a coupling equation:

$D(\theta, \phi) = \vec{F}(\vec{k}) \cdot \overrightarrow{F'}\left(\overrightarrow{k'}\right) = \vec{F}(\vec{k}) \cdot \overrightarrow{F'}\left(-\overrightarrow{k'}\right)$ (3.29)

Put Equation3.26 and 3.28 into Equation 3.29 can obtain:

$D_1(\theta, \phi) = -f_\theta(\theta, \phi) f'_{\theta}(\theta, \pi - \phi) + f_\phi(\theta, \phi) f'_{\phi}(\theta, \pi - \phi)$ (3.30)

Where $f'_{\theta'}, f'_{\phi}$ are probe's far field patterns, which usually are known value. f_θ, f_ϕ are tow unknown value. Then we need second time measurement test, which is polarized $90°$ to the first measurement.

The old $o' - x'y'z'$ coordinate system will rotate $90°$ in figure[3.22],

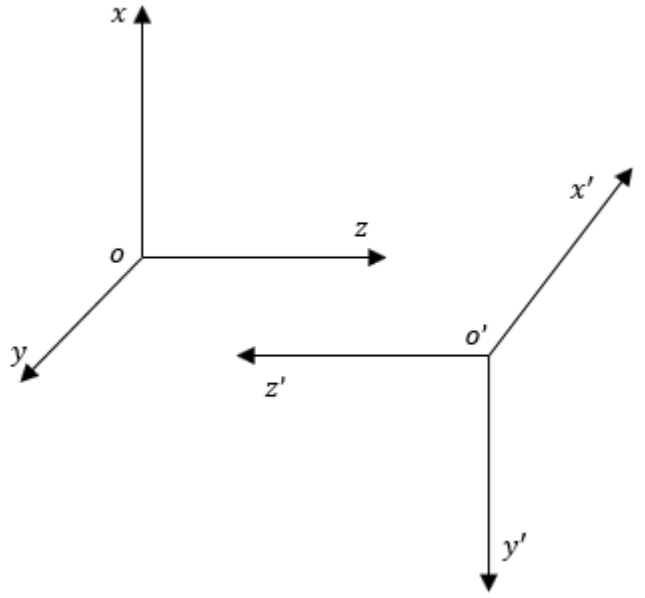

Figure 3.21: Coordinator System of the second measurement after rotating $90°$

then will get new relations:

$\hat{x} = -\widehat{y'}, \hat{y} = -\widehat{x'}, \hat{z} = -\widehat{z'}$

$\theta = \theta', \phi = \frac{\pi}{2} - \phi'$ (3.31)

Use the same reason we can get

$\widehat{\theta'} = -\hat{\theta}$

$\widehat{\phi'} = \hat{\phi}$

$\overrightarrow{k'} = -\vec{k}$

Then get

$D_2(\theta, \phi) = -f_\theta(\theta, \phi) f'_\theta\left(\theta, \frac{\pi}{2} - \phi\right) + f_\phi(\theta, \phi) f'_\phi(\theta, \frac{\pi}{2} - \phi)$ (3.32)

Use inverse Fourier Transform to Equation 3.2 get:

$$D_1(\theta, \phi) = \frac{k_0 \cos\theta}{C} \iint_{S_2} P_{r1}(x, y, d) \exp(j\vec{k} \cdot \overrightarrow{r_0}) \, \mathrm{d}x \, \mathrm{d}y$$

$$= \frac{\cos\theta}{C\lambda} \exp(jkd \cdot cos\theta) I_1(\theta, \phi)$$

The same reason:

$$D_2(\theta, \phi) = \frac{\cos\theta}{C'\lambda} \exp(jkd \cdot cos\theta) I_2(\theta, \phi)$$

$I_{1,2}(\theta, \phi)$ is defined as

$I_{1,2}(\theta, \phi) = \iint_{S_2} P_{r1,2}(x, y, d) \exp[(jk(xsin\theta cos\phi + ysin\theta sin\phi)] dxdy$ (3.33)

P_{r1}, P_{r2} are two probe receiving voltage measurements.

Combine equation 3.30 and equation 3.32 we can get:

$$\begin{cases} f_\theta(\theta,\phi) = \dfrac{\cos\theta}{C'\lambda f_E(\theta)} \exp(jkd \cdot cos\theta) \left[I_1(\theta,\phi) {f'}_\phi \left(\theta, \dfrac{\pi}{2} - \phi\right) - I_2(\theta,\phi) {f'}_\phi(\theta, \pi - \phi) \right] / \Delta(\theta,\phi) \\ f_\phi(\theta,\phi) = \dfrac{\cos\theta}{C'\lambda f_H(\theta)} \exp(jkd \cdot cos\theta) \left[(\theta,\phi) {f'}_\theta \left(\theta, \dfrac{\pi}{2} - \phi\right) - I_2(\theta,\phi) {f'}_\theta(\theta, \pi - \phi) \right] / \Delta(\theta,\phi) \end{cases} \tag{3.34}$$

Where

$$\Delta(\theta,\phi) = [{f'}_\phi(\theta, \pi - \phi) {f'}_\theta \left(\theta, \tfrac{\pi}{2} - \phi\right) - {f'}_\phi \left(\theta, \tfrac{\pi}{2} - \phi\right) {f'}_\theta(\theta, \pi - \phi)] \tag{3.35}$$

The Eq 3.34 can be simplified to these equations below:

$$\begin{cases} f_\theta(\theta,\phi) = \dfrac{\cos\theta}{C'\lambda f_E(\theta)} \exp(jkd \cdot cos\theta) \left[I_1(\theta,\phi) sin\phi - I_2(\theta,\phi) cos\phi \right] \\ f_\phi(\theta,\phi) = \dfrac{\cos\theta}{C'\lambda f_H(\theta)} \exp(jkd \cdot cos\theta) \left[-I_1(\theta,\phi) cos\phi + I_2(\theta,\phi) sin\phi \right] \end{cases} \tag{3.36}$$

So equation (3.34) and equation (3.36) are the far-field pattern in near-field measurements considering the probe compensation.

4

Results and Discussions

This chapter presents the results of this thesis obtained from the implementation and experiments in chapter 3.

4.1 Measurement setup

The measurement setup is done as in Figure 4.1, the cable and connector type that supports the frequency range of the measurements are chosen. Using Electronic calibration (Ecal) module the cables are calibrated. The VNA is set with an input power of 10 dBm, the number of data points to 201. The S11 parameter was measured for both AUT and probe and is presented in Table 4.1.

Table 4.1: S11 values of AUT and Probe

Frequency (GHz)	AUT-S11 (dB)	Probe-S11 (dB)
28	-18.37	-10.56
39	-30.76	-15.91

The scanner is fixed at the bottom of the chamber, the AUT is fixed to a bar which can be moved based on the separation distance. The AUT and probe are aligned so that their coordinates are parallel.

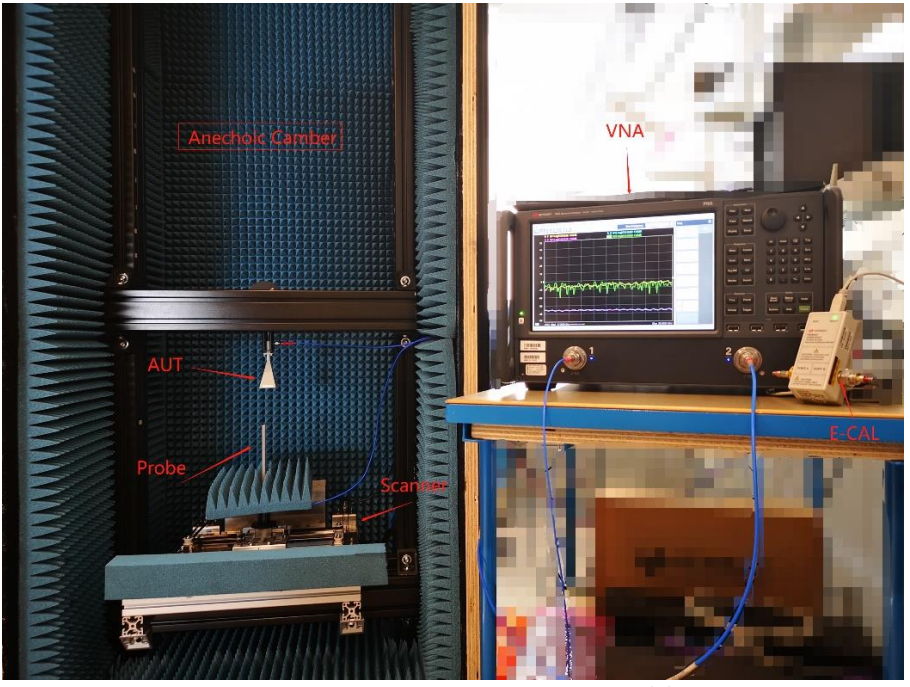

Figure 4.1: Measurement setup at Ericsson lab

The E-Plane and H-plane of the AUT used in the thesis are as shown in Figure 4.2 for 29 GHz and 39 GHz according to the datasheet provided by the manufacturer. The designed near-field system should predict the far-field pattern of AUT as in Figure 4.2.

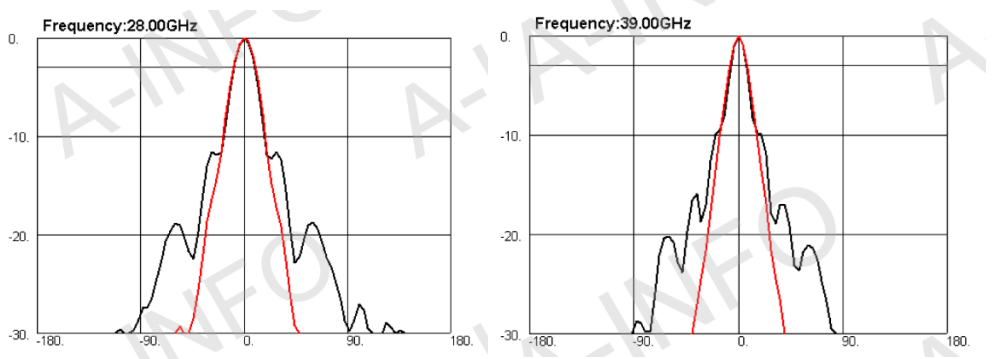

(a) (b)

Figure 4.2: E-plane and H-plane of AUT (a) 28 GHz (b) 39 GHz red curve are H plane and black curve are E plane

4.2 Simulation results for 28 GHz

The measurement setup for frequency 28 GHz is done as follows:

Frequency, $f = 28\ \text{GHz}$

The wavelength, $\lambda = \frac{c}{f} = \frac{3\times10^8}{28\times10^9} = 0.0107\ \text{m}$

AUT diameter, $D = 40.4\ \text{mm}$

Near-field region, $0.62\sqrt{\frac{D^3}{\lambda}} > NF < \frac{2D^2}{\lambda}$, $\quad NF \approx 4.8\ \text{cm-}30.5\ \text{cm}$

So, the separation distance between AUT and probe should be in the range of $5\ \text{cm} - 30\ \text{cm}$. Let the separation distance be, $z = 30\ \text{cm}$ and step size $\Delta x = \Delta y = 4\ \text{mm}$. The maximum scan area that can be achieved based on the step size is 164 mm x 164 mm. So, 41 x 41 values are collected per scan by VNA. The measured near-field data is then transformed into far-field as mentioned in chapter 3.5. The E-plane and H-plane patterns in the following Figure 4.3 are obtained for this measurement setup.

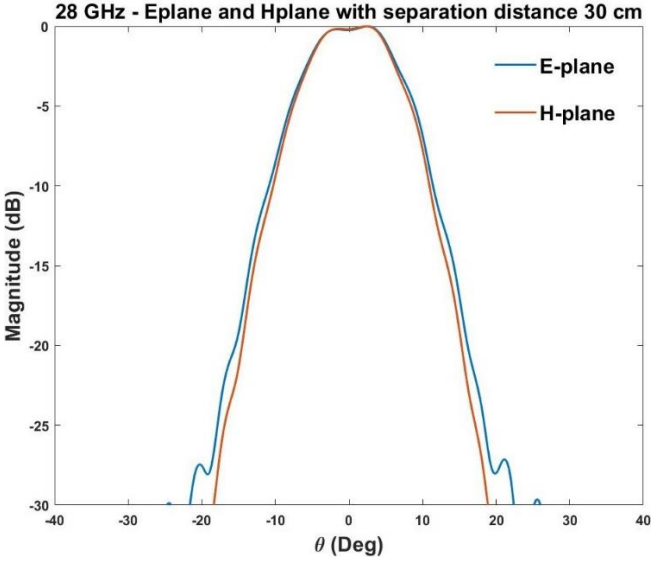

Figure 4.3: Measurement results for 28 GHz E-plane and H-plane

The simulation results E-plane and H-plane for 28 GHz obtained agree with the analytical data in a certain angle range when compared to expected results as shown in Figure 4.2.a. For this configuration, the angle range is $\theta_{\pm} = 11.65°$ calculated from eqn.3.1 and the obtained result was $\theta_{\pm} = 11.3°$, a difference of 0.35° from the expected results was observed. The range will be enlarged, and the results will be much

closer if the size of the scan area is increased. The dip in the E-plane and H-plane results at the top is mainly due to the misalignment of the AUT and the probe.

The simulations were done for different separation distance within the near-field range and it was observed that the angle range was increased as the distance decreases. But, the E-plane and H-plane weren't in good agreement with the expected AUT's pattern. The E-plane and H-plane of AUT for various separation distances are as shown in Figure 4.4 and Figure 4.5 respectively for 28 GHz.

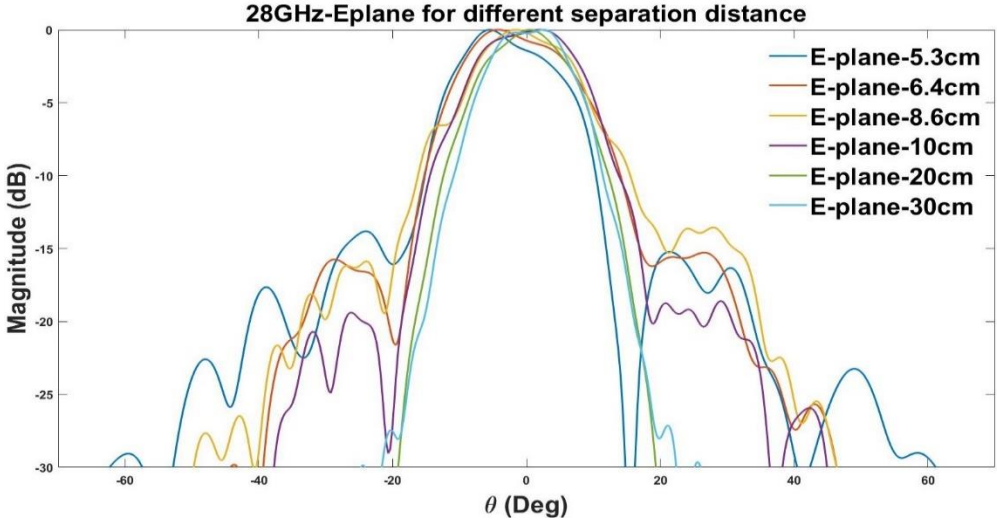

Figure 4.4: Measurement results for 28 GHz E-plane for different separation distance

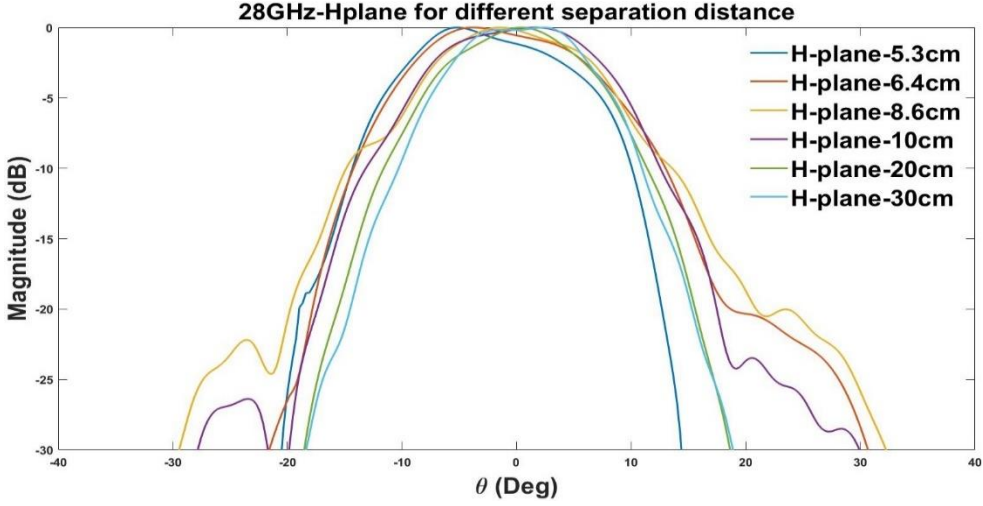

Figure 4.5: Measurement results for 28 GHz H-plane for different separation distance

4.3 Simulation results for 39 GHz

The same AUT as above but change the frequency to 39GHz

The wavelength now is $\lambda = \frac{c}{f} = \frac{3\times10^8}{39\times10^9} = 0.0077\ \mathrm{m}$

With same dimension of AUT we can get the Near-field region, $0.62\sqrt{\frac{D^3}{\lambda}} > NF < \frac{2D^2}{\lambda}$, $NF \approx 5.7\ \mathrm{cm}\text{-}42.4\ \mathrm{cm}$.

Means the distance between AUT and probe in 39GHz measurements now is between 6cm to 42cm. So, choose $z = 10\ \mathrm{cm}$ for the measurements. Due to the smaller wavelength, the step sizer should be smaller so set $\Delta x = \Delta y = 3\ \mathrm{mm}$. The scan area now is 165 mm x 165 mm. So, 55 x 55 values are collected per scan by VNA.

Used the same transform then we get the E-plane and H-plane patterns in the following Figure 4.6 are obtained for this measurement setup.

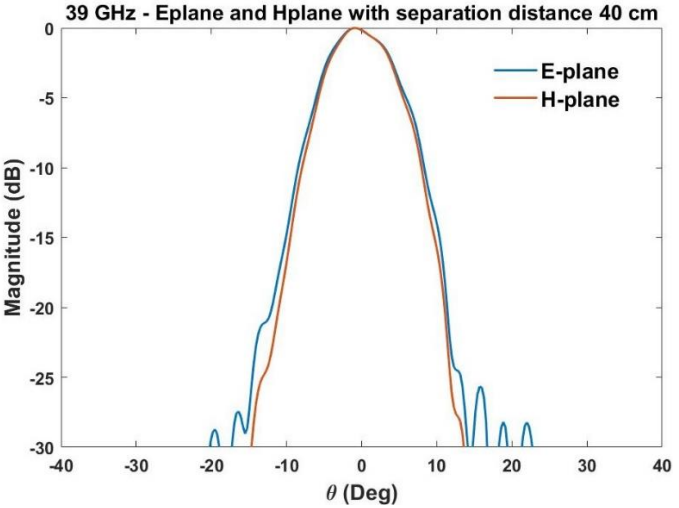

Figure 4.6: Measurement results for 39 GHz E-plane and H-plane of AUT

The simulation results E-plane and H-plane for 39 GHz obtained agree with the analytical data in a certain angle range when compared to expected results as shown in Figure 4.2.a. For this configuration, the angle range is $\theta_{\pm} = 8.85°$ calculated from eqn.3.1 and the obtained result was $\theta_{\pm} = 8.4°$, a difference of 0.45° from the expected results was observed. The range will be enlarged, and the results will be much closer if the size of the scan area is increased. The shift of E-plane and H-plane results from zero degree is mainly due to the misalignment of the AUT and the probe.

The simulations were done for different separation distance within the near-field range and it was observed that the angle range was increased as the distance decreases. But, the E-plane and H-plane weren't in good agreement with the expected AUT's pattern. The E-plane and H-plane for various separation distances are as shown in Figure 4.7 and Figure 4.8 respectively for 39 GHz.

As the distance between the AUT and the probe decreases below 10 cm the results were distorted and were unable to obtain the results. It can be seen from Figure 4.7 and Figure 4.8, the E-plane and the H-plane for 10 cm distance the results deviate much from the expected results.

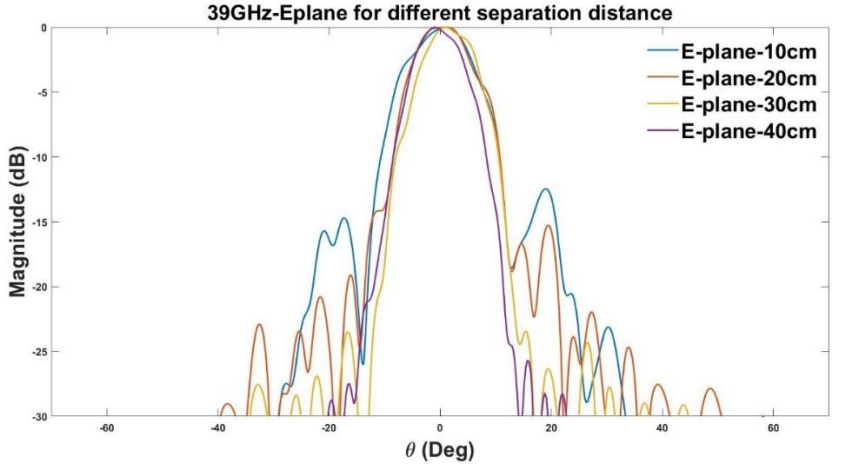

Figure 4.7: Measurement results for 39 GHz E-plane for different separation distance

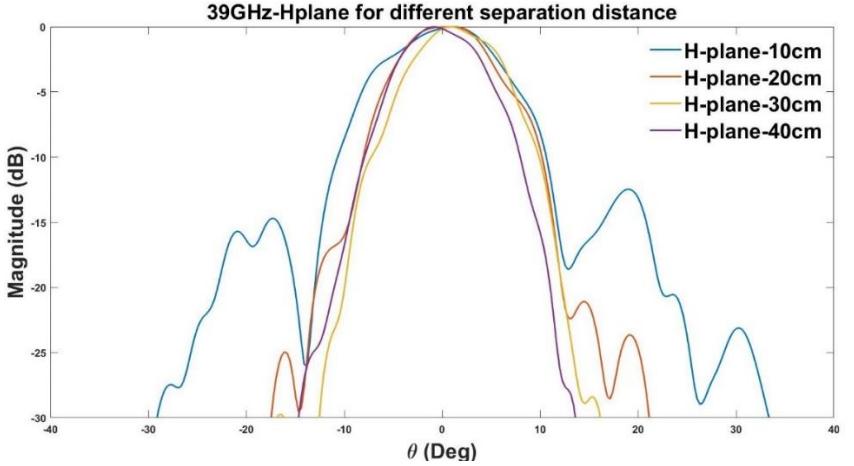

Figure 4.8: Measurement results for 39 GHz H-plane for different separation distance

The measurements were done for variation of sampling values (or step size) of the scanner and input power levels. The change in step size didn't affect the radiation

pattern E-plane and H-plane as shown in Figure 4.9 and Figure 4.10 respectively. It was observed that input power level is important for the better results of the radiation pattern. The results obtained were in good agreement with the expected results with higher input levels. With the input power level of -20 dBm the radiation pattern was distorted as shown in Figure 4.11. and the results obtained were too much deviated when compared to Figure 4.3 in which same configuration was used except with input power of 10 dBm.

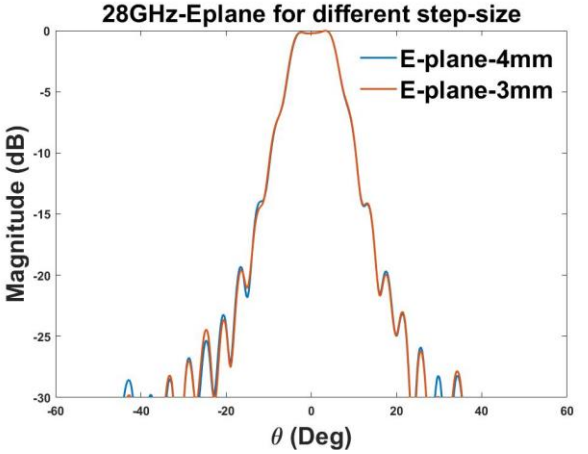

Figure 4.9: Measurement results for 28 GHz E-plane for different step sizes

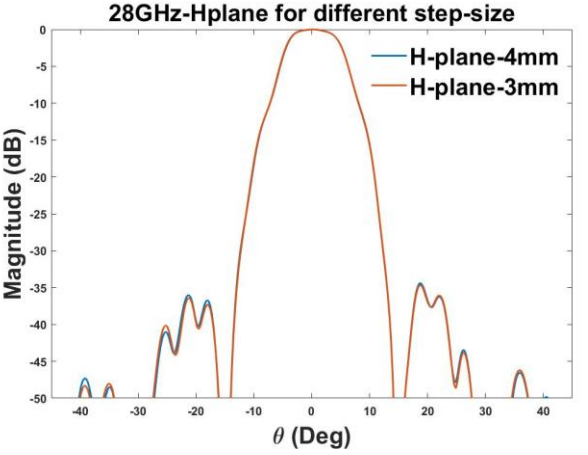

Figure 4.10: Measurement results for 28 GHz H-plane for different step sizes

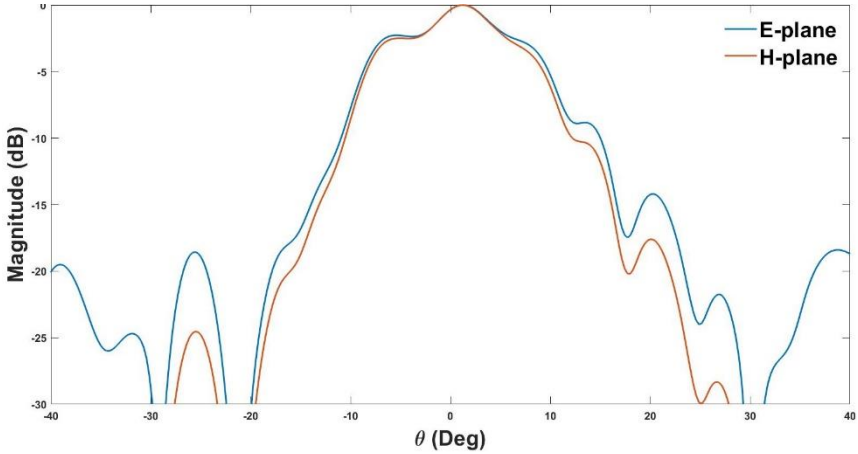

Figure 4.11: Measurement results for 28 GHz E-plane and H-plane with input power -20dBm

4.4 Limitations

There are several limitations for the designed system, few important of them are listed below.

Cable flexing: The stressing of cables, connectors will introduce undesirable variation in amplitude and mainly phase. The receiving cable connected to the probe will be moving continuously and this results in bending of cable, variations in the received data. It was observed during the measurements that frequent changing of cables and connectors provided better results.

Alignment errors: The AUT and probe need to be aligned so their coordinate system is parallel. The antenna alignment is non-mechanically, and this will introduce human error. The probe is rotated by 90° during measurements to obtain second polarization and is done mechanically. Hence care must be taken for proper alignment.

Scanner design: Position errors produce errors in the far-field pattern. The required step size accuracy couldn't be achieved due to the design of the scanner. The scanner area was limited, and it was observed from the simulations higher the scan area higher the angle range and better the results.

VNA: The power level of the VNA instrument depends on the operating frequency range. Two VNA's instruments were used for measurements, one with a frequency range of 10 MHZ-40 GHz with a maximum power level of 0 dBm and another with 10

MHz-67 GHz with a maximum power level of 10 dBm. It was observed there was a difference in results obtained from the two VNA instruments for the same configurations.

5

Conclusion

5.1 Conclusion

The aim of the thesis was to design a near-field antenna measurement system at mm-wavelength to predict the radiation pattern E-plane and H-plane of the antenna. The near-field system was designed for mm-wavelength antenna operational frequency 28 GHz and 39 GHz.

In the near field system, the main parts are the probe, scanner, and near-field to far-field transformation. Based on the literature studies from the technical papers, the type of probe, scanner design, the transformation method were chosen. The WR28 open-ended rectangular waveguide is chosen as a probe, the planar scanning geometric was implemented by designing a scanner of length 165 mm x 175 mm and near-field data are measured at specific points based on the sampling values using Vector Network Analyzer (VNA) in an anechoic chamber. The near-field to far-field transformation is implemented using the Plane Wave Spectrum (PWS) method by Fourier transforms in MATLAB.

The designed near-field antenna measurement system is tested for WR28 standard gain horn antenna as an antenna under test. The near field measurements were performed for antenna operation frequency: 28 GHz and 39 GHz and the far-field pattern E-plane and H-plane were obtained. The difference of 0.2° - 0.5° was observed between the obtained and the expected results. The measurements were performed for different separation distances between the antennas, sampling value, and power level. The results obtained E-plane and H-plane for 28 GHz were more accurate than 39 GHz compared to the expected results. For 39 GHz, as the distance between the AUT and the probe decreases below 10 cm the results were distorted and were unable to obtain the results. Future work has been presented to analyze the problems and propose improvements in both hardware and software.

5.2 Future work

The thesis work has accomplished the objectives, but however, a lot more work could be done with respect to refining the existing design and exploration for newer solutions. After having worked on the designed system for some time now we have found some areas that can be further improved which we didn't have time nor resources to do. Some of the improvements and future work are:

- Improve the measurement system in terms of
  - Increase the scan area.
  - Better alignment of the measurement system by using lasers.
- Test of active antennas.
- Investigate the issues of distorted results obtained for 39 GHz.
- Implement measurement of antenna gain, directivity, etc.
- Analyze the measurement system with other probes and antennas.
- Test of different transformation methods like Huygens's equivalence principle, phaseless measurement method.

For the test of active antenna systems will be more important part of the future work:

Nowadays the active antennas system is popular. Using low-cost sensors and field programmable gates arrays to manipulate the antenna in real time [24]. In telecommunication field, usually when measuring the 5G base station radio, the interface of the AAS usually is the common public radio interface (CPRI) connector, this could be the biggest difference compared to our measurement system now. And, in reality, the 5G AAS the radio has both Tx/Rx, so to achieve a full property of the AAS the measurements should contain both Tx and Rx.
According to (Keisuke, Nozomu, etc.) [24] The simple measurement system should be like in the figure below:

(a) Transmitter measurement

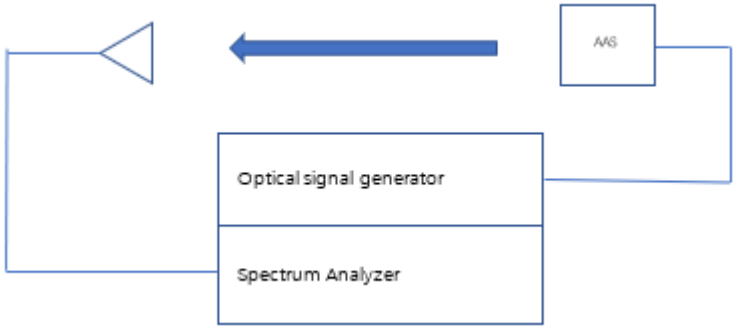

(b) Receiver measurement

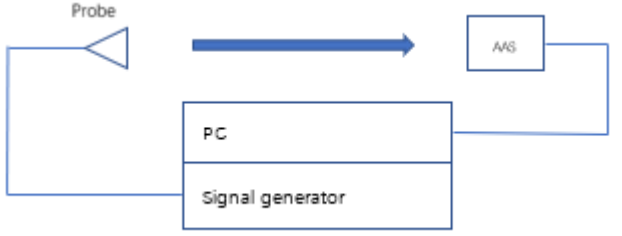

Figure 5.1 AAS measurement system diagram

So, for future AAS measurement, based on our system. The Spectrum analyzer and optical signal generator (CPRI) are needed at least in the system build.

Active antenna performance evaluation

In the transmit mode of the active antenna, each transmitter generates an amplified outgoing high-level signal from an input phase reference signal distributed to each transmitter from a common source. The total transmitted power is in general unrelated to the amplitude of the reference signal. Therefore, the conventional definition of gain is not useful in describing the action of the antenna. Rather we focus on Effective Isotropic Radiated Power or EIRP to quantify the strength of the transmitted wave.

Bibliography

[1] Michael. D. Foegelle, “Antenna Pattern Measurement: Concepts and Techniques”, Compliance Engineering, January 2002.

[2] “Ericsson Mobility Report, Special edition: World Economic Forum” January 2019

[3] White paper “*Advanced antenna systems for 5G networks*”, GFMC-18:000530, Ericsson, November 2018.

URL:*https://www.ericsson.com/en/white-papers/advanced-antenna-systems-for-5g-networks*

[4] Lee Teschler, *"Why 5G is going to over-the-air testing"*, June 21, 2018

[5] Yihong Qi, Guang Yang, Lie Liu, Jun Fan, Antonio Orlandi, Hongwei Kong, Wei Yu, Zhiping Yang, "*5G Over-the-Air Measurement Challenges: Overview*", IEEE Transaction on Electromagnetic Compatibility, May.2017

[6] Antenna standards Committee, 3GPP TR 38.810 "*Study on test methods*", IEEE Antennas and Propagation Society, v16.2.0, March 2019.

[7] C.A. Balanis, "*Antenna Theory- Analysis and Design*", John Wiley, 1997

[8] Jingnan Pan, Xu Gao. Yaojiang Zhang, Jun Fan, "*Far-field radiation estimation from near-field measurements and image theory*," IEEE Transaction on Antennas Propagation, August 2014.

[9] R.M. Barrett and M.H. Barnes, "*Automatic antenna wavefront plotter*," Electron., vol.25, pp. 120-125, Jan. 1952.

[10]D.M. Kerns, "*Analytical techniques for the correction of near-field antenna measurements made with an arbitrary but known measuring antenna*," in Abstracts URSI-IRE Meeting, Washington, DC, April-May 1963, pp.6-7.

[11] D.M. Kerns, "*Correction of near-field antenna measurements made with an arbitrary but known measuring antenna*," Electron. Lett., vol.6, pp.346-347, May 1970.

[12]A.D. Yaghjian, "*An overview of near-field measurements*," IEEE Transactions on Antennas Propagation, vol.AP-34, pp.30-45, Jan.1986.

[13]Wikipedia, www.enwikipedia.org/wiki/Horn_antenna.

[14] IEEE-SA Standards Board, "*IEEE Recommended Practice for Near-Field Antenna Measurements*", IEEE Antennas and Propagation Society1720-2012, Dec.2012.

[15] Ch. Taybi, R.K. Kwate, B. Elmagroud, A. Ziyyat, M.A. Moutaouekkil, "*Probes characterization for antennas near field measurements*," IEEE MMS, Dec.2014.

[16] J.H. Richmond and T.E. Tice, "*Probes for microwave near-field measurements*", IRE Transactions, April 1955.

[17] Newell, A.C, "*Error analysis techniques for planar near-field measurements*," IEEE Trans. on Antenna and Propagation, vol.36, no.6, pp. 754-768, June 1988.

[18] Adafruit learning system. *URL:https://www.learn.adafruit.com (accessed: 2019-09-26)*

[19] Electronics-notes. *URL:https://www.electronics-notes.com(accessed: 2019-09-26)*

[20]A. D. Yaghjian, "*Approximate formulas for the far-field and gain of open-ended rectangular waveguide,*" IEEE Transactions on Antennas Propagation, vol. AP-32, pp. 378-384, Apr. 1984.

[21]NaiHong Mao, Xinde Ju *"Handbook of Antenna Measurement*," Beijing National Defense Industry Press, 1988.

[22]Yu Ding, "*Study of some key problems of planar near-field radiation and scattering measurements*," Ph.D. dissertation, Xidian University, January 2004.

[23] Gregory F. Masters, "Test and Measurement Planning for Active Antennas", 2014 IEEE Conference on Antenna Measurements & Applications (CAMA)

[24] Keisuke Sato, Nozomu Sasaki, Shuta Morinaga, Susumu Miura, Kota Shishido, Yukitaka Takahashi, Katsumori Sasaki, and Ichiro Oshima, "Study of Radiation Characteristic Measurement System of 3.5 GHz Active Antenna System, Proceedings of 2017 IEEE CAMA, Tsukuba, Japan"